

## Anharmonicity in the High-Temperature *Cmcm* Phase of SnSe: Soft Modes and Three-Phonon Interactions

Jonathan M. Skelton, Lee A. Burton, Stephen C. Parker, and Aron Walsh\*  
*Department of Chemistry, University of Bath, Claverton Down, Bath BA2 7AY, United Kingdom*

Chang-Eun Kim and Aloysius Soon  
*Department of Materials Science and Engineering, Yonsei University, Seoul 120-749, Korea*

John Buckeridge, Alexey A. Sokol, and C. Richard A. Catlow  
*University College London, Kathleen Lonsdale Materials Chemistry, Department of Chemistry,  
20 Gordon Street, London WC1H 0AJ, United Kingdom*

Atsushi Togo and Isao Tanaka  
*Elements Strategy Initiative for Structural Materials, Kyoto University, Kyoto Prefecture 606-8501, Japan*  
(Received 13 January 2016; published 10 August 2016)

The layered semiconductor SnSe is one of the highest-performing thermoelectric materials known. We demonstrate, through a first-principles lattice-dynamics study, that the high-temperature *Cmcm* phase is a dynamic average over lower-symmetry minima separated by very small energetic barriers. Compared to the low-temperature *Pnma* phase, the *Cmcm* phase displays a phonon softening and enhanced three-phonon scattering, leading to an anharmonic damping of the low-frequency modes and hence the thermal transport. We develop a renormalization scheme to quantify the effect of the soft modes on the calculated properties, and confirm that the anharmonicity is an inherent feature of the *Cmcm* phase. These results suggest a design concept for thermal insulators and thermoelectric materials, based on dispersive instabilities, and highlight the power of lattice-dynamics calculations for materials characterization.

DOI: [10.1103/PhysRevLett.117.075502](https://doi.org/10.1103/PhysRevLett.117.075502)

Thermoelectrics are an important class of functional materials which interconvert heat and electricity [1], and are a key component in the drive for “green” energy [2]. The figure of merit for thermoelectric performance is  $ZT = S^2\sigma T / (\kappa_L + \kappa_{el})$ , where  $S$  and  $\sigma$  are the Seebeck coefficient and electrical conductivity, and  $\kappa_L$  and  $\kappa_{el}$  are the lattice and electronic thermal conductivities, respectively. The key to developing high-performance thermoelectric materials is to reduce the thermal conductivity while maintaining a high thermopower  $S^2\sigma$ . Widespread application requires a  $ZT$  above 2 at the target operating temperature [3].

Historically, the lead chalcogenides set the benchmark for high thermoelectric performance due to their unique combination of favorable electrical properties and strongly anharmonic lattice dynamics [4–11]. However, bulk SnSe was recently shown to be a very promising high-temperature thermoelectric, with a  $ZT$  score surpassing the record set by nanostructured PbTe [12]. This has been ascribed to an ultralow lattice thermal conductivity, arising from its pseudolayered structure and strong high-temperature

anharmonicity [13,14]. Compared to PbTe, SnSe achieves superior thermoelectric performance without the need for doping or other material modifications [15], which can be detrimental to electrical properties. It is therefore important to elucidate the microscopic origin of its high performance, in order that the same ideas may be incorporated into design strategies for improving thermoelectrics.

SnSe displays a second-order phase transition from *Pnma* to *Cmcm* phases between 700–800 K [13,14]. Modeling studies on the thermal transport of the low-temperature phase have been carried out [16], while combined theoretical and computational studies of both phases [14,17] have connected the low lattice thermal conductivity to the anharmonicity arising from the dispersive phase transition. However, there has not yet been a detailed comparison of the intrinsic lattice dynamics of the two phases, in part due to the difficulties associated with modeling phonon instabilities.

Previous theoretical studies have shown that first-principles lattice-dynamics calculations can provide deep insight into the material physics underlying thermoelectric performance [18–25]. In this work, we have employed first-principles lattice-dynamics calculations to model both phases of SnSe, with a particular focus on characterizing the lattice dynamics and thermal transport in the high-temperature phase, and on developing a practical approach

---

Published by the American Physical Society under the terms of the [Creative Commons Attribution 3.0 License](https://creativecommons.org/licenses/by/3.0/). Further distribution of this work must maintain attribution to the author(s) and the published article's title, journal citation, and DOI.

to the theoretical challenge of modeling soft-mode instabilities.

Our lattice-dynamics calculations were performed using the Phonopy [26,27] and Phono3py [28] packages, with the VASP code [29] as the force calculator. We used the PBEsol functional [30], which we have previously found to give a very good description of the lattice dynamics in a range of semiconductors [31]. Projector augmented-wave (PAW) pseudopotentials [32,33] treating the Sn 4*d*, 5*s*, and 5*p* and the Se 4*s* and 4*p* electrons as valence were used to model the ion cores. The electronic wave functions were expanded in a plane-wave basis with a kinetic-energy cutoff of 500 eV. An  $8 \times 4 \times 8$  Monkhorst-Pack *k*-point mesh was used to sample the Brillouin zone, correspondingly reduced for the supercell force calculations [34]. The second-order (harmonic) force constants were computed using a carefully chosen  $6 \times 1 \times 6$  supercell expansion for both phases and a displacement step of  $10^{-2}$  Å. The third-order force constants were computed using  $3 \times 1 \times 3$

expansions and a  $3 \times 10^{-2}$  Å step. Full technical details of our simulations, along with supercell-size convergence tests for the harmonic-phonon calculations, can be found in the Supplemental Material [35].

The optimized equilibrium structures of the two phases are shown in Figs. 1(c) and 1(d). The calculated lattice parameters of the *Pnma* and *Cmcm* phases are  $a = 4.367$ ,  $b = 11.433$ , and  $c = 4.150$  Å, and  $a = 4.217$  Å,  $b = 11.525$ , and  $c = 4.204$  Å, respectively. These values are consistent with experimental characterization (*Pnma*:  $a = 4.44$  Å,  $b = 11.49$  Å,  $c = 4.135$  Å; *Cmcm*:  $a, c = 4.31$  Å,  $b = 11.70$  Å), and with other theoretical studies [13,16]. The low-temperature phase is a distortion of the more symmetric high-temperature structure, leading to a primitive unit cell with twice the volume, and both structures can be thought of as distortions to the rocksalt structure of the Pb analogue PbSe.

Comparing the phonon dispersion and density-of-states (DOS) curves of the two phases [Figs. 1(a) and 1(b)], the

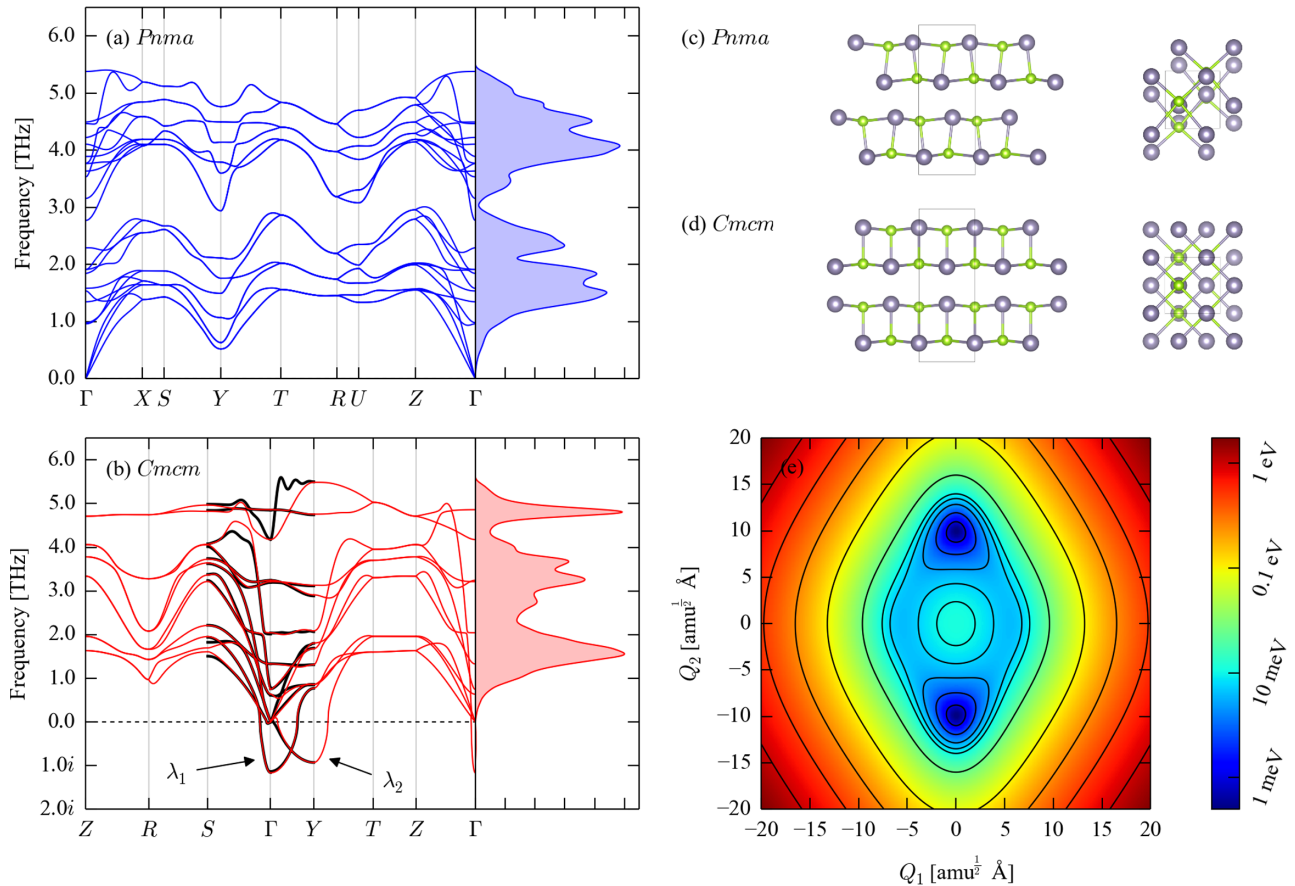


FIG. 1. Lattice dynamics of SnSe. Plots (a) and (b) show the phonon dispersions and densities of states of the optimized equilibrium *Pnma* and *Cmcm* structures illustrated in (c) and (d), respectively. The dispersion of the high-temperature *Cmcm* phase shows imaginary modes at the symmetry points  $\Gamma$  and  $Y$ , marked  $\lambda_1$  and  $\lambda_2$ , respectively. The black lines in the *Cmcm* dispersion are segments computed from supercells chosen to have a larger number of commensurate points along the corresponding reciprocal-space directions (Ref. [35]). The 2D potential-energy surface along the two corresponding normal-mode coordinates ( $Q_1/Q_2$ ) is shown in plot (e). The left- and right-hand snapshots in (c) and (d) are taken through the *ab* and *ac* planes, respectively, and the Sn and Se atoms in the models are colored silver and green. The images were prepared using VESTA (Ref. [39]).

upper-frequency part of the  $Cmcm$  DOS displays a noticeable redshift with respect to the  $Pnma$  phase. From a numerical integration [35], around 15% of the states in the low-temperature phase lie between 3–4 THz, compared to  $\sim 30\%$  in the high-temperature phase. Moreover, whereas the dispersion of the  $Pnma$  structure shows real frequencies across the Brillouin zone [Fig. 1(a)], the dispersion of the high-temperature phase displays prominent imaginary modes along the line between  $\Gamma$  and  $Y$  [Fig. 1(b)], with the primary soft modes at the two symmetry points [14,17].

The imaginary modes make an almost negligible contribution to the overall phonon DOS, suggesting them to be confined to a small reciprocal-space volume. This was confirmed by inspecting the frequencies at the commensurate  $\mathbf{q}$ -points in the various supercells used for convergence testing, as well as in a set of  $2 \times N \times 2$  expansions with a high density of commensurate points along the  $\Gamma$ - $Y$  line [35].

From an analysis of the phonon eigenvectors [35], both modes correspond to symmetry-breaking displacive instabilities. The optic mode at  $\Gamma$  corresponds to motion of the four (two) Sn and Se atoms in the conventional (primitive) cell in opposing directions parallel to the  $c$  axis. The acoustic mode at  $Y$  is a similar motion along the  $a$  axis, but with the atoms in the two bonded layers moving in opposite directions. From mapping out the 2D potential-energy surface spanned by the two mode eigenvectors [Fig. 1(e)], it can be seen that the  $Y$  mode represents the primary distortion to the low-temperature phase: the minimum along the  $\Gamma$ -point mode [ $\lambda_1$  in Fig. 1(b) and  $Q_1$  in Fig. 1(e)] is another saddle point on this potential-energy surface, whereas the global energy minimum lies along the  $Y$  mode ( $\lambda_2/Q_2$ ). It can also be seen from a comparison of the  $Pnma$  and  $Cmcm$  structures in Figs. 1(c) and 1(d) that the symmetry breaking induced by this mode maps between the high-temperature to the low-temperature phase.

Each imaginary mode forms an anharmonic double-well potential [Figs. 2(a) and 2(c)]. The potential along the  $\Gamma$ -point mode is steeper, accounting for its more negative harmonic frequency, but, as seen in Fig. 1(e), the potential along the  $Y$  mode possesses a deeper minimum. The respective minima are both shallow, at 5 and 11 meV below the average structure. These findings indicate that the  $Cmcm$  phase is effectively an average structure, in a manner analogous to the high-temperature phases of some oxides [40] and oxide and halide perovskites (e.g.,  $\text{CsSnI}_3$ ) [25,41,42]. To confirm that the  $Cmcm$  phase is unlikely to become stable under lattice expansion (or contraction) at finite temperature, we computed phonon dispersions and DOS curves over a range of expansions and contractions about the athermal equilibrium volume [35], which indicated that the imaginary modes soften further under lattice expansion, and also persist under moderate applied pressure.

Soft modes present a challenge to lattice-dynamics calculations, as techniques for treating this anharmonicity

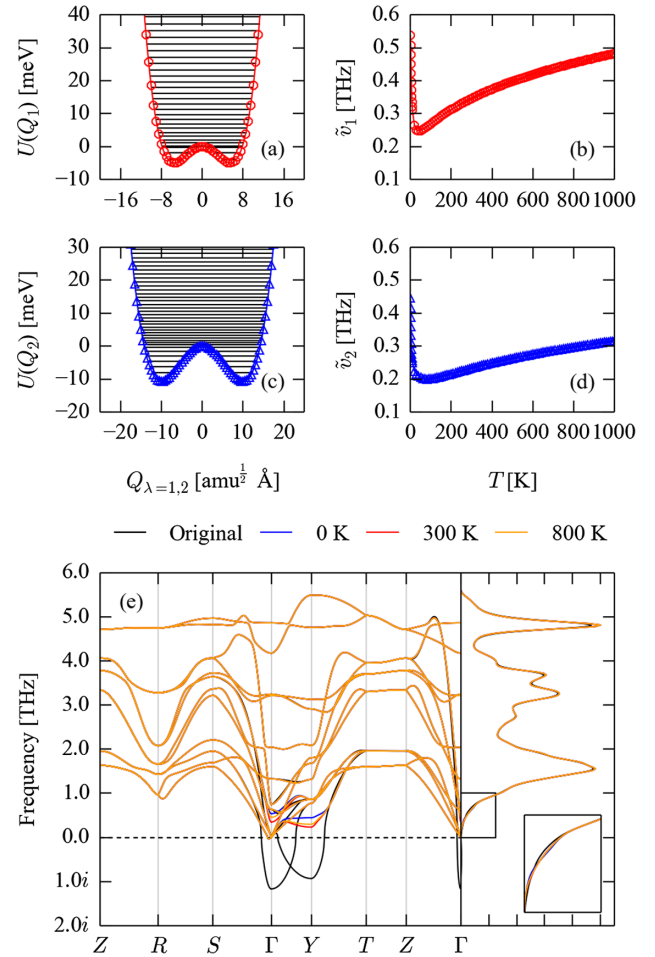


FIG. 2. Renormalization of the imaginary harmonic-phonon modes in the equilibrium  $Cmcm$  SnSe structure. Plots (a) and (c) show the anharmonic double-well potentials along the two modes labeled  $\lambda_1$  and  $\lambda_2$  in Fig. 1(b) as a function of the corresponding normal-mode coordinates  $Q_{\lambda=1,2}$ . The markers show the calculated points, the solid lines are fits to a 20-power polynomial, and the black lines inside the potentials show the eigenvalues obtained by solving a 1D Schrödinger equation. Plots (b) and (d) show the effective renormalized frequencies of the two modes ( $\tilde{\nu}_{\lambda=1,2}$ ) as a function of temperature, calculated as the harmonic frequencies which reproduce the contributions of the modes to the vibrational partition function. Plot (e) compares phonon dispersions and densities of states calculated without renormalization (black) and with the imaginary modes renormalized to the calculated 0 (blue), 300 (red), and 800 K (orange) frequencies.

(e.g., self-consistent phonon theory [43,44]) are often impractically expensive. Whereas in real systems phonon instabilities are localized to regions of infinitesimal volume in reciprocal space (i.e., points, lines, or planes), and thus do not contribute to thermodynamic properties such as the free energy [40], the finite Brillouin-zone sampling and interpolation used in lattice-dynamics calculations “spreads” the imaginary modes over a finite volume.

In order to investigate the effect of the imaginary modes in the high-temperature phase on our calculations, we

implemented a simple renormalization scheme to calculate approximate effective harmonic frequencies. The potential energy along each mode as a function of the respective normal-mode coordinate,  $Q_{\lambda=1,2}$ , is fitted to a 20-power polynomial and 1D Schrödinger equations for the potentials are solved to obtain the eigenvalues inside the anharmonic double wells [Figs. 2(a) and 2(c)]. Effective (real) harmonic frequencies for the imaginary modes are then calculated as a function of temperature to reproduce the contribution of the modes to the anharmonic vibrational partition function [Figs. 2(b) and 2(d)]. These effective frequencies are used to adjust the harmonic force constants, by back transforming the dynamical matrices at the commensurate  $\mathbf{q}$ -points in the supercell expansion after adjusting the frequencies of the imaginary modes. The corrected force-constant matrices are then used as input for further postprocessing. A detailed overview of the renormalization scheme and its implementation is given in the Supplemental Material [35].

The  $\Gamma$  and  $Y$  points in the  $Cmcm$  primitive cell are commensurate with our chosen  $6 \times 1 \times 6$  supercell expansion, but the expansion has no commensurate points along the  $\Gamma$ - $Y$  line. The dispersion appears to be well reproduced with this expansion [cf. Fig. 1(b)], however, and it was thus employed for renormalization at the symmetry points. The renormalized 0 K frequencies of the imaginary modes at  $\Gamma$  and  $Y$  are 0.54 and 0.45 THz, respectively. The frequencies initially decrease with temperature, as the system explores higher energy levels within the minima, and reaches a minimum close to where the available thermal energy is comparable to the barrier height (approx. 40 and 80 K, respectively, for the two modes). Above these temperatures, the renormalized frequencies increase monotonically as the system accesses the steeper parts of the potential. The renormalized frequencies at 300 K are 0.35 ( $\Gamma$ ) and 0.23 THz ( $Y$ ), and increase to 0.45 ( $\Gamma$ ) and 0.30 THz ( $Y$ ) at 800 K (the temperature above which the  $Cmcm$  phase is observed crystallographically [13,14]).

Figure 2(e) shows the impact of renormalizing the imaginary modes at 0, 300, and 1000 K on the phonon dispersion and DOS. The effect on the orthogonal phonon branches is minimal, and the correction is strongly localized to the lines along which the imaginary modes occur. The latter is primarily a result of the large supercell used for calculating the force constants, which we consider a prerequisite for this renormalization scheme. The effect of the renormalization on the phonon DoS is minimal, with the most notable differences occurring up to  $\sim 1$  THz [Fig. 2(e), inset].

The renormalization was also found to have a negligible impact on thermodynamic functions calculated within the harmonic approximation [35], with a maximum difference in the high-temperature (1000 K) vibrational Helmholtz free energy of  $< 0.3$  kJ mol $^{-1}$  per SnSe formula unit ( $\sim 0.3\%$ ; cf.  $k_B T = 8.314$  kJ mol $^{-1}$  at this temperature).

To investigate the effect of the phase transition on the thermal transport, we modeled the phonon lifetimes within the single-mode relaxation-time approximation, which were used to solve the Boltzmann transport equations. The lifetimes are calculated as the phonon self-energy within many-body perturbation theory, using the three-phonon interaction strengths  $\phi_{\lambda\lambda\lambda'}$ , obtained from the third-order force constants  $\phi_{\alpha\beta\gamma}$  along with an expression for the conservation of energy. This method is implemented in the `Phono3py` code, and a detailed overview may be found in Ref. [28]. In these calculations, we did not attempt to correct the third-order force constants for the imaginary modes in the  $Cmcm$  phase, but instead performed post-processing for the high-temperature structure using renormalized second-order force constants.

Neglecting quasiharmonic effects from volume expansion,  $\phi_{\lambda\lambda\lambda'}$  is temperature independent, and a histogram showing the average phonon-phonon interaction strengths,  $P_{\mathbf{q}j}$ , across the phonon DOS [Figs. 3(a)–3(c)] provides a convenient means to compare the inherent “anharmonicity” of the two phases. This comparison clearly shows that the low-frequency modes in the  $Cmcm$  phase experience a substantially stronger interaction with other phonon modes compared to the lower-frequency branches in the  $Pnma$  phase. Correcting the second-order force constants reduces the interaction strength up to  $\sim 0.5$  THz, but the average  $P_{\mathbf{q}j}$  up to  $\sim 3$  THz remains consistently higher than in the  $Pnma$  phase. These calculations therefore indicate that the lattice dynamics of the high-temperature phase are inherently more anharmonic.

The calculated 300 K lattice thermal conductivity ( $\kappa_L$ ) of the  $Pnma$  phase [Fig. 3(d)] is 1.43, 0.52, and 1.88 W m $^{-1}$  K $^{-1}$  along the  $a$ ,  $b$ , and  $c$  axes, respectively. These values are in reasonable agreement with measurements of  $\sim 0.7$  and  $\sim 0.45$  W m $^{-1}$  K $^{-1}$  along the two short and one long axes [13], and the predicted axial anisotropy is consistent with other studies [13,16]. For the  $Cmcm$  phase [Fig. 3(e)], we calculated an isotropic average  $\kappa_L$  of 0.33 W m $^{-1}$  K $^{-1}$  at 800 K compared to the measured value of  $\sim 0.25$  W m $^{-1}$  K $^{-1}$  [13]. Given the neglect of volume expansion, higher-order anharmonicity, and other potential scattering processes in the present calculations, this is again reasonable agreement. As in the  $Pnma$  phase, the calculations predict an axial anisotropy in  $\kappa_L$ , with significantly reduced transport along the long axis. With the second-order force constants corrected, we calculated an average  $\kappa_L$  of 0.34 (an increase of 2.4%), indicating that renormalization has only a small quantitative impact. Analysis of the modal contributions to the thermal transport at 300 and 800 K [35] shows that the low-frequency modes account for the bulk of the heat transport in both phases, and that the larger phonon-phonon interaction strengths in the  $Cmcm$  phase significantly reduce the lifetimes of these modes, thus explaining its reduced  $\kappa_L$ .

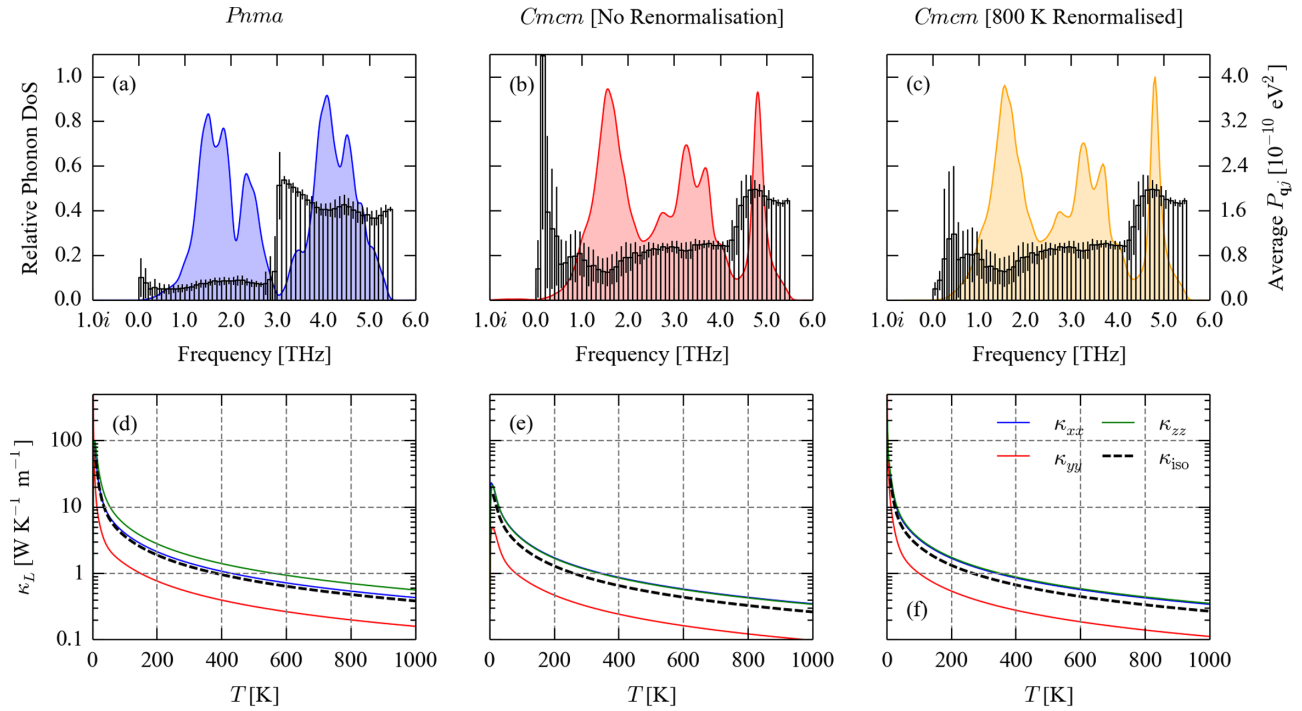


FIG. 3. Thermal-transport properties of the  $Pnma$  (a),(d) and  $Cmcm$  (b),(c),(e),(f) phases of SnSe. Plots (a)–(c) show the averaged three-phonon interaction strengths,  $P_{qj}$  (as defined in Ref. [28]), overlaid on the phonon densities of states. The error bars show the standard deviation on the average in each histogram bin. Plots (d)–(e) show the calculated lattice thermal conductivity ( $\kappa_L$ ) along each of the three crystallographic axes, together with the isotropic average. The  $Cmcm$ -phase data shown in (b) and (e) was modeled without renormalization of the imaginary modes, while that shown in (c) and (f) was modeled with the second-order (harmonic) force constants corrected using the 800 K renormalized frequencies.

These findings are consistent with the mechanism proposed in Refs. [14,17]. Our calculations show that the high-temperature phase exhibits a substantial phonon softening compared to the  $Pnma$  phase, and that enhanced phonon-phonon interactions in the  $Cmcm$  phase lead to an anharmonic damping of the low-frequency modes and hence the thermal transport. Moreover, our renormalization scheme provides a means to explore the physics of the soft modes and their effect on calculated properties, such as the thermodynamic free energy and the thermal transport, from first principles, without requiring experimental measurements of the phonon frequencies to fit to [14].

In this regard, our scheme could easily be combined with the quasiharmonic approximation, which would allow us to explore the effect of thermal expansion at finite temperature. This would be expected to further dampen the thermal conductivity [24], and detailed lattice-dynamics calculations could allow the relative contributions from changes in phonon lifetimes and group velocities to be discerned [14].

In summary, our calculations demonstrate that the low high-temperature lattice thermal conductivity of SnSe is due to anharmonic damping of the low-frequency phonon modes. We have developed a simple renormalization scheme to quantify the impact of the phonon instabilities in the high-temperature phase on properties calculated

using second-order force constants, and hence shown the enhanced anharmonicity to be an inherent property of this system. This scheme may form a practical basis for studying other important classes of system with displacive instabilities, e.g., halide perovskites. From a materials-design perspective, similar anharmonic phonon dampening may occur in other systems at the boundary of a phase transition, and so this could serve as a selection criterion for identifying materials with ultralow thermal conductivity [14]. In these materials, the poor thermal transport is a bulk property, and so the potential negative impact on electrical properties of modifications such as doping and nanostructuring may be avoided. Understanding this phenomenon may thus provide a robust design strategy for developing thermal insulators and high-performance thermoelectric materials.

In addition to the data in the Supplemental Material [35], the optimized structures and raw or processed data from the phonon calculations can be obtained by following the link in Ref. [45]. This also includes the codes used to implement our approximate renormalization scheme.

We gratefully acknowledge helpful discussions with Dr J. M. Frost. J. M. S. is supported by an EPSRC programme grant (Grant No. EP/K004956/1). L. A. B. is currently supported by the JSPS (Grant No. 26.04792).

J.B. acknowledges support from the EPSRC (Grant No. EP/K016288/1). Calculations were carried out on the ARCHER supercomputer, accessed through membership of the UK HPC Materials Chemistry Consortium, which is funded by the EPSRC (Grant No. EP/L000202). We also made use of the Bath University HPC cluster, which is maintained by the Bath University Computing Services, and the SiSu supercomputer at the IT Center for Science (CSC), Finland, via the Partnership for Advanced Computing in Europe (PRACE) Project No. 13DECI0317/IsoSwitch.

\* a.walsh@bath.ac.uk

- [1] J. R. Sootsman, D. Y. Chung, and M. G. Kanatzidis, *Angew. Chem., Int. Ed.* **48**, 8616 (2009).
- [2] G. J. Snyder and E. S. Toberer, *Nat. Mater.* **7**, 105 (2008).
- [3] J. F. Li, W. S. Liu, L. D. Zhao, and M. Zhou, *NPG Asia Mater.* **2**, 152 (2010).
- [4] R. N. Tauber, A. A. Machonis, and I. B. Cadoff, *J. Appl. Phys.* **37**, 4855 (1966).
- [5] Y. Z. Pei, X. Y. Shi, A. LaLonde, H. Wang, L. D. Chen, and G. J. Snyder, *Nature (London)* **473**, 66 (2011).
- [6] Z. M. Gibbs, H. Kim, H. Wang, R. L. White, F. Drymiotis, M. Kaviani, and G. Jeffrey Snyder, *Appl. Phys. Lett.* **103**, 262109 (2013).
- [7] E. S. Bozin, C. D. Malliakas, P. Souvatzis, T. Proffen, N. A. Spaldin, M. G. Kanatzidis, and S. J. L. Billinge, *Science* **330**, 1660 (2010).
- [8] O. Delaire *et al.*, *Nat. Mater.* **10**, 614 (2011).
- [9] S. Kastbjerg, N. Bindzus, M. Sondergaard, S. Johnsen, N. Lock, M. Christensen, M. Takata, M. A. Spackman, and B. B. Iversen, *Adv. Funct. Mater.* **23**, 5477 (2013).
- [10] T. Keiber, F. Bridges, and B. C. Sales, *Phys. Rev. Lett.* **111**, 095504 (2013).
- [11] K. S. Knight, *J. Phys. Condens. Matter* **26**, 385403 (2014).
- [12] K. Biswas, J. Q. He, I. D. Blum, C. I. Wu, T. P. Hogan, D. N. Seidman, V. P. Dravid, and M. G. Kanatzidis, *Nature (London)* **489**, 414 (2012).
- [13] L.-D. Zhao, S.-H. Lo, Y. Zhang, H. Sun, G. Tan, C. Uher, C. Wolverton, V. P. Dravid, and M. G. Kanatzidis, *Nature (London)* **508**, 373 (2014).
- [14] C. W. Li, J. Hong, A. F. May, D. Bansal, S. Chi, T. Hong, G. Ehlers, and O. Delaire, *Nat. Phys.* **11**, 1063 (2015).
- [15] J. P. Heremans, *Nature (London)* **508**, 327 (2014).
- [16] J. Carrete, N. Mingo, and S. Curtarolo, *Appl. Phys. Lett.* **105**, 101907 (2014).
- [17] J. Hong and O. Delaire, *arXiv:1604.07077v2*.
- [18] J. M. An, A. Subedi, and D. J. Singh, *Solid State Commun.* **148**, 417 (2008).
- [19] A. H. Romero, M. Cardona, R. K. Kremer, R. Lauck, G. Siegle, J. Serrano, and X. C. Gonze, *Phys. Rev. B* **78**, 224302 (2008).
- [20] Y. Zhang, X. Z. Ke, C. F. Chen, J. Yang, and P. R. C. Kent, *Phys. Rev. B* **80**, 024304 (2009).
- [21] O. Kilian, G. Allan, and L. Wirtz, *Phys. Rev. B* **80**, 245208 (2009).
- [22] T. Shiga, J. Shiomi, J. Ma, O. Delaire, T. Radzynski, A. Lusakowski, K. Esfarjani, and G. Chen, *Phys. Rev. B* **85**, 155202 (2012).
- [23] Z. T. Tian, J. Garg, K. Esfarjani, T. Shiga, J. Shiomi, and G. Chen, *Phys. Rev. B* **85**, 184303 (2012).
- [24] J. M. Skelton, S. C. Parker, A. Togo, I. Tanaka, and A. Walsh, *Phys. Rev. B* **89**, 205203 (2014).
- [25] J. Buckeridge, D. O. Scanlon, A. Walsh, C. R. A. Catlow, and A. A. Sokol, *Phys. Rev. B* **87**, 214304 (2013).
- [26] A. Togo, F. Oba, and I. Tanaka, *Phys. Rev. B* **78**, 134106 (2008).
- [27] A. Togo and I. Tanaka, *Scr. Mater.* **108**, 1 (2015).
- [28] A. Togo, L. Chaput, and I. Tanaka, *Phys. Rev. B* **91**, 094306 (2015).
- [29] G. Kresse and J. Hafner, *Phys. Rev. B* **47**, 558 (1993).
- [30] J. P. Perdew, A. Ruzsinszky, G. I. Csonka, O. A. Vydrov, G. E. Scuseria, L. A. Constantin, X. L. Zhou, and K. Burke, *Phys. Rev. Lett.* **100**, 136406 (2008).
- [31] J. M. Skelton, D. Tiana, S. C. Parker, A. Togo, I. Tanaka, and A. Walsh, *J. Chem. Phys.* **143**, 064710 (2015).
- [32] P. E. Blochl, *Phys. Rev. B* **50**, 17953 (1994).
- [33] G. Kresse and D. Joubert, *Phys. Rev. B* **59**, 1758 (1999).
- [34] H. J. Monkhorst and J. D. Pack, *Phys. Rev. B* **13**, 5188 (1976).
- [35] See Supplemental Material at <http://link.aps.org/supplemental/10.1103/PhysRevLett.117.075502> for a detailed computational protocol, convergence tests and additional data including a description of our renormalization scheme and an analysis of the thermal conductivities of the two phases, which includes Refs. [36–38].
- [36] K. Parlinski, Z.-Q. Li, and Y. Kawazoe, *Phys. Rev. Lett.* **78**, 4063 (1997).
- [37] B. S. Garbow, *Comput. Phys. Commun.* **7**, 179 (1974).
- [38] J. Buckeridge and S. Fahy, *Phys. Rev. B* **84**, 144120 (2011).
- [39] K. Momma and F. Izumi, *J. Appl. Crystallogr.* **44**, 1272 (2011).
- [40] M. T. Dove, *Am. Mineral.* **82**, 213 (1997).
- [41] L.-Y. Huang and W. R. L. Lambrecht, *Phys. Rev. B* **90**, 195201 (2014).
- [42] E. L. da Silva, J. M. Skelton, S. C. Parker, and A. Walsh, *Phys. Rev. B* **91**, 144107 (2015).
- [43] N. R. Werthamer, *Phys. Rev. B* **1**, 572 (1970).
- [44] I. Errea, M. Calandra, and F. Mauri, *Phys. Rev. B* **89**, 064302 (2014).
- [45] See <https://github.com/WMD-group/Phonons>.